JGR Space Physics

RESEARCH ARTICLE
10.1029/2024JA032984

Key Points:

- Electron precipitation likely driven by electromagnetic ion cyclotron (EMIC) waves is observed within 1–2 hr of electron flux dropouts
- Pitch angle diffusion rates inferred from low altitude measurements allow estimating the contribution of EMIC wave-driven losses to dropouts
- EMIC wave-driven electron precipitation could significantly modulate electron flux dropouts above 1.5 MeV and sometimes down to 0.5 MeV

Supporting Information:

Supporting Information may be found in the online version of this article.

Correspondence to:

D. Mourenas,
didier.mourenas@cea.fr

Citation:

Mourenas, D., Artemyev, A. V., Zhang, X.-J., & Angelopoulos, V. (2024). Impact of EMIC waves on electron flux dropouts measured by GPS spacecraft: Insights from ELFIN. *Journal of Geophysical Research: Space Physics*, *129*, e2024JA032984. https://doi.org/10.1029/2024JA032984

Received 18 JUN 2024
Accepted 13 SEP 2024

Impact of EMIC Waves on Electron Flux Dropouts Measured by GPS Spacecraft: Insights From ELFIN

Didier Mourenas[1,2], Anton V. Artemyev[3], Xiao-Jia Zhang[3,4], and Vassilis Angelopoulos[3]

[1]CEA, DAM, DIF, Arpajon, France, [2]Laboratoire Matière en Conditions Extrêmes, CEA, Université Paris-Saclay, Bruyères-le-Châtel, France, [3]Department of Earth, Planetary, and Space Sciences, University of California, Los Angeles, Los Angeles, CA, USA, [4]Department of Physics, University of Texas at Dallas, Richardson, TX, USA

Abstract Although the effects of electromagnetic ion cyclotron (EMIC) waves on the dynamics of the Earth's outer radiation belt have been a topic of intense research for more than 20 years, their influence on rapid dropouts of electron flux has not yet been fully assessed. Here, we make use of contemporaneous measurements on the same *L*-shell of trapped electron fluxes at 20,000 km altitude by Global Positioning System (GPS) spacecraft and of trapped and precipitating electron fluxes at 450 km altitude by Electron Losses and Fields Investigation (ELFIN) CubeSats in 2020–2022, to investigate the impact of EMIC wave-driven electron precipitation on the dynamics of the outer radiation belt below the last closed drift shell of trapped electrons. During six of the seven selected events, the strong 1–2 MeV electron precipitation measured at ELFIN, likely driven by EMIC waves, occurs within 1–2 hr from a dropout of relativistic electron flux at GPS spacecraft. Using quasi-linear diffusion theory, EMIC wave-driven pitch angle diffusion rates are inferred from ELFIN measurements, allowing us to quantitatively estimate the corresponding flux drop based on typical spatial and temporal extents of EMIC waves. We find that EMIC wave-driven electron precipitation alone can account for the observed dropout magnitude at 1.5–3 MeV during all events and that, when dropouts extend down to 0.5 MeV, a fraction of electron loss may sometimes be due to EMIC waves. This suggests that EMIC wave-driven electron precipitation could modulate dropout magnitude above 1 MeV in the heart of the outer radiation belt.

1. Introduction

Electromagnetic ion cyclotron (EMIC) waves are recorded in the inner magnetosphere under disturbed geomagnetic conditions (Blum et al., 2017; Ross et al., 2021; X.-J. Zhang, Li, Thorne, et al., 2016). They are generated by anisotropic hot ion populations injected from the plasma sheet or produced by magnetosphere compression (H. Chen et al., 2020; McCollough et al., 2010; Remya et al., 2018). EMIC waves in the hydrogen band often reach high amplitudes ~ 1 nT in the noon-dusk sector (Ross et al., 2021; X.-J. Zhang, Li, Thorne, et al., 2016). They can efficiently scatter electrons in pitch angle toward the loss cone through cyclotron resonance near the equator, leading to their rapid precipitation into the atmosphere (Blum et al., 2015; Sandanger et al., 2007; Summers & Thorne, 2003; Thorne & Kennel, 1971; Usanova et al., 2014). Therefore, EMIC waves can control the dynamics of trapped electron fluxes in the Earth's outer radiation belt, through a strong and abrupt reduction of electron lifetimes above ~ 1 MeV compared to situations with whistler-mode hiss or chorus waves but without EMIC waves (Kersten et al., 2014; Li et al., 2007; Ni et al., 2015), as confirmed by spacecraft observations both within and outside the plasmasphere (Mourenas et al., 2017; Mourenas et al., 2021; X.-J. Zhang et al., 2017).

Conjugate observations of EMIC waves near the magnetic equator and electron precipitation at low altitude have confirmed the high efficiency of this electron loss mechanism above $\sim 1 - 2$ MeV, but also demonstrated the presence of simultaneous electron precipitation at lower energy, down to about ~ 0.3 MeV (Angelopoulos et al., 2023; Capannolo et al., 2019; Hendry et al., 2017; X.-J. Zhang et al., 2021). This low energy electron precipitation by EMIC waves was initially surprising, because the condition of cyclotron resonance with such low energy electrons requires both a high plasma density and EMIC waves with much larger wave number and frequency than the typical frequency of peak wave power in observations, probably in the hydrogen band because hot plasma effects apparently prevent resonance with such low energy electrons in the helium band (Angelopoulos et al., 2023; L. Chen et al., 2013). Statistics of EMIC wave power from the Van Allen Probes have shown the presence of a finite tail of wave power at high frequencies nearly up to the proton gyrofrequency (X.-J. Zhang, Li, Thorne, et al., 2016; X. Shi et al., 2024), which can indeed account for the full observed energy spectrum of electron precipitation by EMIC waves (An et al., 2024; Angelopoulos et al., 2023).

Several theoretical and observational studies have suggested that EMIC wave-driven electron precipitation could significantly contribute to dropouts of relativistic electron flux in the heart of the outer radiation belt, which consist of rapid (<10-hr) and important (by more than a factor of $2-3$) decreases of near-equatorial electron flux that mainly occur above $\sim 1-2$ MeV (Boynton et al., 2017; Mourenas et al., 2016; Xiang et al., 2018; X. J. Zhang, Li, Ma, et al., 2016). Observations of deepening minima of electron phase space density (PSD) during dropouts are consistent with an important contribution of EMIC waves to such dropouts of multi-MeV electrons (Drozdov et al., 2022; Shprits et al., 2017; Xiang et al., 2018).

In the present paper, we use trapped electron flux measurements from the Combined X-ray and Dosimeter (CXD) instrument on board Global Positioning System (GPS) spacecraft on orbit at 20,000 km altitude with a 55° inclination (Morley et al., 2016, 2017), which allow for a 2-hr resolution, and simultaneous measurements of precipitating and trapped electron fluxes by Electron Losses and Fields Investigation (ELFIN) mission CubeSats on a polar orbit at 450 km altitude (Angelopoulos et al., 2020). We select events with a strong precipitating-to-trapped electron flux ratio >0.25 peaking above 1 MeV at ELFIN, a telltale signature of EMIC wave-driven electron precipitation (Angelopoulos et al., 2023), and check their potential impact on trapped electron fluxes at $\sim 0.2-2$ MeV measured by GPS spacecraft on the same L-shells. We only keep events with ELFIN observations of such characteristic EMIC wave signatures at L-shells significantly lower than the minimum last closed drift shell (LCDS) of trapped electrons, to exclude as much as possible an immediate effect of outward electron loss (Albert et al., 2018; Olifer et al., 2021; Yu et al., 2012). The magnitude of electron flux dropouts recorded by GPS spacecraft during the selected events is compared with the expected magnitude of EMIC wave-driven dropouts, estimated based on the corresponding electron pitch angle diffusion rates inferred from ELFIN measurements, allowing us to quantitatively check the potential contribution of EMIC waves to such dropouts.

2. Analysis of the Impact of Strong EMIC Wave-Driven MeV Electron Loss at ELFIN on Electron Flux Dropouts at GPS Spacecraft

2.1. Events Selection

The main goal of the present study is to examine variations of trapped electron flux measured by GPS spacecraft at $200-2000$ keV at a given, relatively high, equatorial pitch-angle $\alpha_{eq,GPS}$ on a given L, in the presence of a burst of intense EMIC waves identified by a precipitating-to-trapped electron flux ratio $j_{prec}/j_{trap} > 0.25$ above 1 MeV, but much smaller at low energies $0.2-0.3$ MeV, recorded by ELFIN CubeSats at low altitude on the same L-shell (Angelopoulos et al., 2023).

Due to the high efficiency of EMIC wave-driven electron pitch-angle scattering toward the loss cone, a sudden decrease of GPS trapped electron flux is expected to occur close in time to the EMIC wave burst, at energies and equatorial pitch-angles for which cyclotron resonance with EMIC waves is possible (Kersten et al., 2014; Usanova et al., 2014). For an ideal quasi-monochromatic EMIC wave at fixed frequency, this decrease of GPS trapped electron flux is expected to occur at high $\alpha_{eq,GPS}$ only at high electron energy. But in the more realistic case of intense H-band EMIC wave packets with a high-frequency wave power tail (Angelopoulos et al., 2023; X. Shi et al., 2024), a direct interaction of EMIC waves through cyclotron resonance with electrons at high $\alpha_{eq,GPS}$ is possible, and it can potentially lead to a decrease of the GPS trapped electron flux over a wide energy range (above ~ 200 keV), although the flux decrease should still remain more important at higher electron energy.

However, another important mechanism of electron loss may be simultaneously present: magnetopause shadowing, which takes place when the magnetosphere is compressed by the solar wind and the magnetopause comes closer to the Earth, allowing outward electron losses on open geomagnetic field lines (Morley et al., 2010; Olifer et al., 2021; Shprits et al., 2006; Turner et al., 2013; West, 1979; Yu et al., 2012). The minimum L-shell down to which this mechanism of electron flux dropout can directly occur is called the minimum LCDS (Albert et al., 2018; Yu et al., 2012). An estimate of the minimum $LCDS$ location, denoted min($LCDS$), can be obtained using the LANL* neural network (Yu et al., 2012) with the TS05 magnetic field model (Tsyganenko & Sitnov, 2005). In the present study, it has been calculated from 12 hr before and up to 2 hr after the recording of strong EMIC wave-driven MeV electron precipitation by ELFIN. It provides an estimate of the minimum L-shell where outward electron loss due to magnetopause shadowing and outward radial diffusion by ULF waves could

Table 1

Date, Hour (UT) of ELFIN Observations of EMIC Wave-Driven Electron Precipitation, Their L-Shell Range, Minimum LCDS Estimated by LANL Neural Network, Times (in Hours From the Beginning of the Day) of Minimum LCDS and $1-2$ MeV Electron Flux Dropout Measured by Global Positioning System (GPS) Spacecraft, Maximum Equatorial Pitch-Angle $\alpha_{eq,GPS}$ at GPS Spacecraft, MLT and Minimum $L_{pp}(Kp)$ (O'Brien & Moldwin, 2003) at ELFIN When No Plasmaspheric Plume is Present, Storm Phase (M for Main, R for Recovery) and Average Dst (in nT) During the 2 hr Following ELFIN Observations, and Maximum Solar Wind Dynamic Pressure P_{dyn} (in nPa) and Kp Index During the 3 hr Preceding ELFIN Observations*

Date (ELFIN)	L	$LCDS$	$t_{LCDS}, t_{dropout}$	$\alpha_{eq,GPS}$	MLT	L_{pp}	Phase $/Dst$	P_{dyn}	Kp
2020-11-02, 15:19	$6.5-7.0$	9.1	6, 16	22°	11:30	4.5	R/ − 8	1.4	0
2021-03-13, 0:40	$4.5-5.0$	6.0	−0:22, 0	54°	18	4.5	R/ − 3	6.7	3
2021-04-19, 3:55	$6.0-6.6$	7	−2:10, 4	25°	16	4.3	M/ − 27	4.6	3.7
2021-09-08, 4:18	$4.1-4.5$	7	−0:10, 3	70°	11:30	3.8	R/ + 3	3.7	4
2022-02-27, 10:50	$4.9-5.5$	6.0	8, 10	46°	16:50	4.1	R/ − 2	6.2	3.7
2022-04-14, 11:30	$4.8-5.2$	5.9	6–10, 10	50°	15:40	3.9	M/ − 19	4.8	4.7
2022-05-01, 13:08	$5.4-5.6$	7.2	1:30, --	33°	15:30	3.7	R/ − 9	1.5	1.7

have immediately occurred during GPS electron flux observations. However, electron outward radial diffusion by ULF waves toward the minimum $LCDS$ may allow a subsequent electron loss down to lower L-shells, about $\sim 0.5-1$ Earth radius lower than min($LCDS$), nearly down to the plasmapause after several hours of intense ULF wave activity (Pinto et al., 2020; Turner et al., 2013). Such outward electron loss is stronger and more frequent above ~ 1 MeV where it can produce a steeper dropout of relativistic electron flux (Boynton et al., 2016, 2017) than at 200–500 keV—quite similarly to EMIC wave-driven electron loss (Angelopoulos et al., 2023).

Dropouts of electron flux due to magnetopause shadowing can occur just before (or after) EMIC wave bursts and, therefore, can be mistaken for EMIC wave-driven electron loss. However, electron losses due to magnetopause shadowing and EMIC wave-driven precipitation can also occur concurrently, leading to steeper dropouts of relativistic electron flux than when only one of these two mechanisms is operating alone (Bruno et al., 2022; Xiang et al., 2017). A previous statistical study of electron flux dropouts at $L \sim 4.2$ observed by GPS satellites has indeed suggested that a combination of magnetopause shadowing and EMIC wave-driven electron losses is probably frequent in the heart of the outer radiation belt (Boynton et al., 2017), with EMIC wave-driven loss modulating the magnitude of the full dropout. EMIC wave generation near noon is indeed favored by solar wind dynamic pressure impulses (H. Chen et al., 2020; Ross et al., 2021), which compress the magnetosphere and simultaneously reduce min($LCDS$).

In the present study, we focus on seven events in 2020–2022 (see Table 1), which have been selected using the following criteria: (a) ELFIN measurements of strong electron precipitation with $j_{prec}/j_{trap} > 0.25$ above 1 MeV together with a much smaller j_{prec}/j_{trap} below 0.3 MeV (a telltale signature of EMIC wave-driven precipitation) performed at $L \in [4, 7]$ where GPS spacecraft measure electron fluxes at not too low equatorial pitch-angles, (b) the L-shells of ELFIN observations must be approximately $\sim 0.5-2.5$ Earth radii lower than the minimum $LCDS$, and (c) the difference between the average Dst during the two hours following ELFIN observations and the average Dst from -12 hr to -4 hr before ELFIN observations must remain less than 20 nT. The criterion (c) should ensure that the adiabatic Dst effect on the variation of the average electron flux between these two periods (before and after ELFIN observations) remains weak (Kim & Chan, 1997). This variation of the average flux will be used below for estimating the magnitude of flux dropouts. Therefore, the flux dropouts obtained through this selection procedure should likely correspond to dropouts of electron phase space density (PSD). We did not attempt to estimate the PSD from GPS omnidirectional flux measurements, because this would require using both an empirical magnetic field model and an empirical electron pitch-angle distribution (PAD) model (Kalliokoski et al., 2023), which could lead to large errors during our particular events, since EMIC wave-driven electron precipitation can strongly modify the PAD at low to moderate equatorial pitch-angles $\approx 20° - 50°$ compared with an empirical PAD model (Usanova et al., 2014).

During these events, the magnetopause location given by the Shue et al. (1998) empirical model, based on solar wind dynamic pressure P_{dyn} and North-South interplanetary magnetic field (IMF) component B_z, was close to

$\sim\min(LCDS)+2$ (Albert et al., 2018). Here, L-shell values are estimated as the mean of L(TS05) and L(dip) (calculated using TS05 and dipolar magnetic field models, respectively) when they are close to each other (i.e., for a weakly disturbed geomagnetic field), and as L(TS05) otherwise.

Among these seven selected events, six events led to a significant decrease of the average electron flux recorded by GPS spacecraft at the same L-shells as ELFIN observations during the two ensuing hours, compared with the initial electron flux averaged between −12 and −4 hr before ELFIN observations (this averaging is performed to mitigate natural oscillations of the flux). Such flux dropouts took place during the main or recovery phase of a moderate geomagnetic storm. The 2 hr following ELFIN observations correspond to a moderate average Dst similar to the average Dst from −12 to −4 hr before ELFIN observations. During these six events, the maximum dropout of $1-2$ MeV electron flux (i.e., the minimum flux) recorded by GPS spacecraft occurred ~ 0 to 10 hr (on average ~ 3 hr) after the time of minimum $LCDS$, at L-shells about 0.5–2.5 Earth radii lower than the estimated $\min(LCDS)$ but still above the minimum plasmapause location $L_{pp}(Kp)$ estimated using an empirical model (O'Brien & Moldwin, 2003) valid in the absence of a plasmaspheric plume.

These results suggest that the actual minimum $LCDS$ could have been lower than estimated by the LANL* neural network and/or outward radial diffusion could have been sufficiently rapid to transport such MeV electrons from low L-shells above the minimum plasmapause location, up to the minimum $LCDS$. During one event, on 1 May 2022, there were ELFIN observations of EMIC wave-driven electron precipitation without any flux dropout in GPS data up to 2 MeV.

Table 1 further indicates that the minimum of $1-2$ MeV electron flux at GPS spacecraft occurred between ~ 90 min before and ~ 40 min after (on average ~ 30 min before) the strong EMIC wave-driven electron precipitation above 1 MeV observed by ELFIN. This burst of intense EMIC waves is probably produced by the solar wind dynamic pressure impulses that compressed the magnetosphere around the time of minimum $LCDS$, leading to transverse ion heating and efficient noon-side H-band EMIC wave generation (H. Chen et al., 2020; Jun et al., 2021). Indeed, a significant peak of solar wind dynamic pressure reaching $P_{dyn}\in[3.7, 6.7]$ nPa was recorded less than 3 hr before ELFIN observations during five of the seven events in Table 1. These EMIC waves may also have been generated by ion injections occurring simultaneously with <300 keV electron injections recorded by GPS spacecraft at those times. But for all events in Table 1, except for the first and last events, the occurrence rate of H-band EMIC waves derived from Van Allen Probes statistics (Ross et al., 2021) is higher for the corresponding (L, P_{dyn}) range than for the corresponding (L, Kp) range given in Table 1. This suggests a more probable EMIC wave generation through magnetosphere compression during these five events. It is likely also the case for the first event in Table 1, with $Kp=0$ and ELFIN observations at 11:30 MLT. During the last event in Table 1, however, Kp and P_{dyn} are similarly low, suggesting that both magnetosphere compression and ion injections played a role in generating EMIC waves near 15:30 MLT.

All the observed flux dropouts in Table 1 took $\sim 2-4$ hr to reach the minimum flux. Since the typical duration of EMIC wave bursts driven by magnetosphere compression in the noon-dusk sector is of the order of $\sim 1-4$ hr (Angelopoulos et al., 2023; Blum et al., 2017, 2020; Usanova et al., 2008), and since the EMIC wave-driven electron precipitation recorded by ELFIN occurred less than 1.5 hr away from the time of minimum electron flux observed at GPS spacecraft during these events, the concomitant generation of EMIC waves may have increased electron loss and modulated the dropout magnitude and its extension in L-shells, as suggested by a previous statistical study (Boynton et al., 2017). Therefore, although EMIC waves may not be the main driver of such $1-2$ MeV electron flux dropouts, they could significantly contribute to such strong electron losses in the immediate aftermath of magnetosphere compression and $LCDS$ minimum.

2.2. A Typical Event

Figure 1 shows a typical event from Table 1, which took place on 27 February 2022. Figures 1a and 1b indicate that there was a solar wind dynamic pressure impulse reaching $P_{dyn}\sim 6$ nPa (black curve), and an North-South IMF component B_z reaching ~ -13 nT (blue curve), near 8:00 UT on 27 February, during the main phase of a moderate geomagnetic storm with a minimum $SYM-H\sim -37$ nT (green curve). The $LCDS$ calculated using the LANL* neural network with the TS05 magnetic field model decreased from $L\sim 11$ to $L\sim 6$ at 8 UT (purple curve). At nearly the same time, a dropout of omnidirectional relativistic electron fluxes was recorded by GPS spacecraft near the magnetic equator at $L=4.9-5.5$ in Figure 1c, which reached its full magnitude near 10 UT.

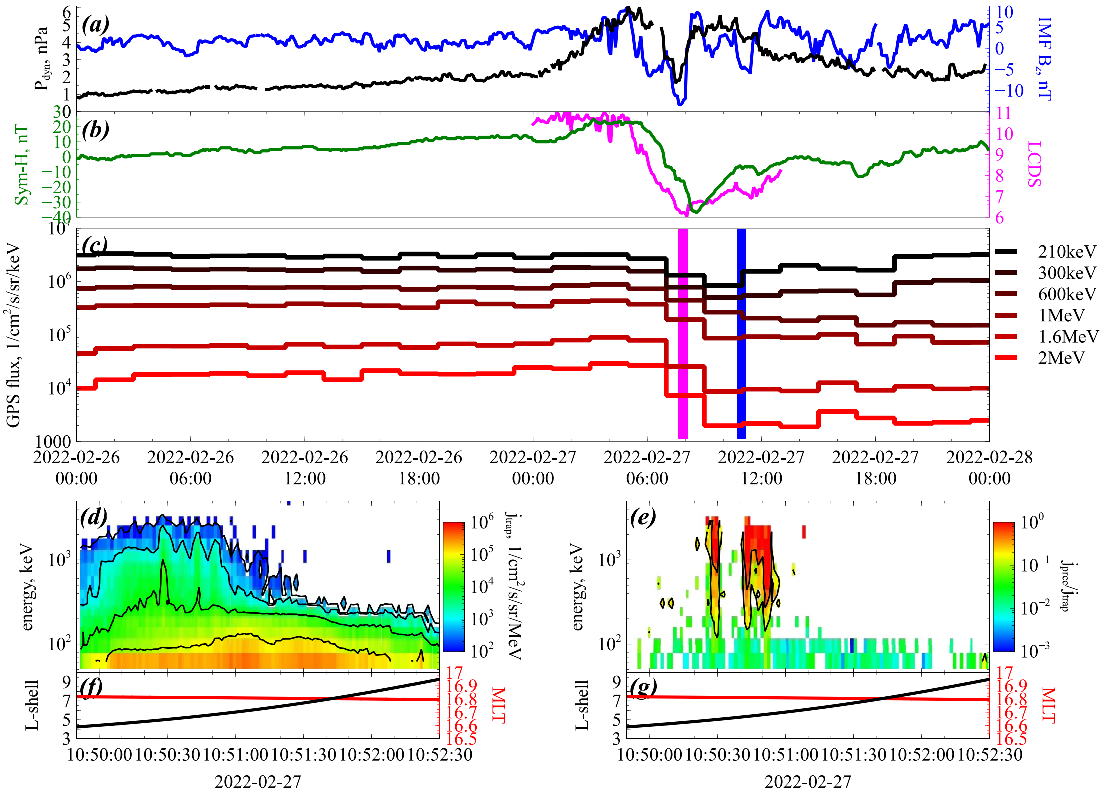

Figure 1. (a) Solar wind dynamic pressure P_{dyn} (black) and Interplanetary magnetic field component B_z (blue). (b) $SYM-H$ index (green) and $LCDS$ (purple) around dropout time calculated with the LANL* neural network, during the 26–27 February 2022 event. (c) Electron fluxes recorded by Global Positioning System spacecraft at $L = 4.9 - 5.5$ during this event. The times of minimum $LCDS$ and of ELFIN observations are indicated by vertical purple and blue lines, respectively. (d) Trapped electron fluxes measured by ELFIN. (e) Ratio j_{prec}/j_{trap} of precipitating to trapped electron fluxes measured at low altitude by ELFIN. (f and g) MLT location (red) and L-shell (black) of ELFIN calculated using the TS05 magnetic field model.

Part of this decrease of electron fluxes between 7 and 10 UT can be attributed to the Dst effect, which can temporarily lead to an adiabatic flux decrease during the main phase of a storm, followed by an increase back to the initial flux level when Dst (or equivalently, $SYM-H$) recovers to its initial nearly null level (Kim & Chan, 1997). Here, Figure 1b shows that at 11–13 UT, $SYM-H$ has already risen back to nearly 0 nT, a level roughly comparable to its initial level from 0 UT on 26 February to 7 UT on 27 February. Therefore, the magnitude of the net flux loss during this dropout can be determined by comparing the average final flux measured by GPS spacecraft at 11–13 UT (i.e., during the 2 hr following ELFIN observations) with the average initial flux between 23 UT on 26 February and 7 UT on 27 February (i.e., from −12 to −4 hr before ELFIN observations), indicating a net drop of $0.6-2$ MeV electron fluxes by factors of $\sim 1/4$ to $1/10$, but a marginal decrease of 200 keV flux.

ELFIN measurements of trapped and precipitating electron fluxes, performed at 10:50 UT on the same L-shells at low altitude (450 km) and 16:50 MLT, are displayed in Figures 1d and 1e, with the corresponding L-shell and MLT indicated in Figure 1f. In particular, Figure 1e shows the ratio of precipitating to trapped electron fluxes, j_{prec}/j_{trap}, measured by the two ELFIN CubeSats, demonstrating intense $1-2$ MeV electron precipitation almost reaching the strong diffusion regime $j_{prec}/j_{trap} \approx 1$ (Kennel, 1969) at $L \simeq 4.9-5.5$ in the noon-dusk sector, with much lower j_{prec}/j_{trap} at lower energies. This is a telltale signature of EMIC wave-driven electron precipitation (Angelopoulos et al., 2023).

During this event, the electron flux dropout recorded by GPS spacecraft at $L = 4.9-5.5$ started at 8 UT, nearly at the time when the $LCDS$ reached its minimum value min($LCDS$) $\simeq 6$, and $0.2-2$ MeV electron fluxes measured by GPS spacecraft near the magnetic equator reached their minimum level roughly 2 hr later, nearly simultaneously with ELFIN observations of intense EMIC wave-driven $0.2-2$ MeV electron precipitation into the atmosphere on the same L-shells. Since such EMIC waves were located in the noon-dusk sector during a geomagnetic storm, and since intense electron precipitation was observed down to ~ 0.2 MeV, it is probable that this low-energy electron precipitation by EMIC waves occurred at the plasmasphere boundary or inside a high density plasmaspheric plume, where cyclotron resonance between low-energy electrons and typical H-band EMIC waves is allowed by a high plasma frequency to gyrofrequency ratio $f_{pe}/f_{ce} > 10 - 15$ (Angelopoulos et al., 2023). Therefore, this 27 February 2022 event suggests that intense EMIC wave-driven electron precipitation may contribute to dropouts of $\sim 0.5 - 2$ MeV electron flux initially caused by magnetopause shadowing, possibly helping their extension to L-shells well below the minimum $LCDS$. Figures S1–S6 in Supporting Information S1 show observations in the same format as in Figure 1 for the six other events in Table 1.

2.3. EMIC Wave-Driven Electron Pitch Angle Diffusion Rates Inferred From ELFIN Measurements

In the following, we estimate the potential contribution of EMIC wave-driven electron losses to the observed flux dropouts. First, it is useful to estimate the maximum equatorial pitch-angle $\alpha_{eq,GPS}$ of electrons detected by GPS satellites. GPS spacecraft provide omnidirectional electron flux data (Morley et al., 2016, 2017). As the local geomagnetic field strength $B(L)$ is available in GPS spacecraft data files, we use it below to infer the time-averaged maximum value, denoted $\alpha_{eq,GPS}$, of $\alpha_{eq} = \sin^{-1}((B/B_{eq}))^{1/2}$ in each case (again using the TS05 magnetic field model). The omnidirectional electron flux in the outer radiation belt is usually dominated by the flux near this maximum equatorial pitch-angle, because (a) the PAD usually exhibits a maximum at $\alpha_{eq} \sim 60° - 90°$ below 2 MeV (Gannon et al., 2007; Greeley et al., 2024; R. Shi et al., 2016; Zhao et al., 2018; Ozeke et al., 2022) and (b) the $\sin \alpha_{eq}$ factor within the integral of the directional flux that gives the omnidirectional flux (e.g., see Roederer, 1970) assigns a higher weight to higher α_{eq} values.

Next, we assume that electrons detected by ELFIN near the equatorial loss cone angle $\alpha_{eq,LC}$ at various energies E_{ELFIN} are precipitated into the atmosphere through cyclotron resonance with left-hand polarized parallel H-band EMIC waves near the equator, where such waves are mostly present (Saikin et al., 2015; H. Chen et al., 2019). This is a reasonable assumption, because H-band EMIC waves often reach sufficiently high frequencies and wave numbers for resonant interaction with 0.2–2 MeV electrons (Angelopoulos et al., 2023; An et al., 2024; Ross et al., 2021; X. Shi et al., 2024; X.-J. Zhang, Li, Thorne, et al., 2016; X.-J. Zhang et al., 2021), whereas hot plasma effects close to the helium gyrofrequency should prevent an efficient scattering of <2 MeV electrons by helium band EMIC waves (Cao et al., 2017; L. Chen et al., 2013; X.-J. Zhang et al., 2021). We further assume that electron transport toward the loss cone can be approximately described by quasi-linear diffusion theory, which is expected to remain approximately valid in the presence of mainly short intense EMIC wave packets and wave superposition (Angelopoulos et al., 2023; X. Shi et al., 2024), as in the case of intense chorus wave packets (Artemyev et al., 2022).

Making use of previous approximate analytical formulations (validated by numerical calculations) of the bounce-averaged quasi-linear diffusion rate $D_{\alpha\alpha}$ of electrons by H-band EMIC waves (Angelopoulos et al., 2023; Mourenas et al., 2016), we can estimate the diffusion rate of electrons detected at GPS spacecraft, $D_{\alpha\alpha}(\alpha_{eq,GPS}, E_{GPS})$, for cyclotron resonance with the same waves (of same frequency) at (E_{GPS}, $\alpha_{eq,GPS}$) and (E_{ELFIN}, $\alpha_{eq,LC}$), based on the diffusion rate $D_{\alpha\alpha}(\alpha_{eq,LC}, E_{ELFIN})$ inferred from ELFIN measurements of precipitating (averaged within the loss cone) and trapped (just above the loss cone) electron fluxes on the same magnetic field line. Analytical estimates show that, as long as cyclotron resonance is possible with the same wave, $D_{\alpha\alpha}$ varies with electron energy and equatorial pitch-angle like $D_{\alpha\alpha} \propto 1/\left(\gamma\, p\, \cos^2 \alpha_{eq}\right)$, with γ the relativistic Lorentz factor and p the electron momentum (Angelopoulos et al., 2023; Mourenas et al., 2016). For electrons of different energies and equatorial pitch-angles $\alpha_{eq} \leq 70°$ in cyclotron resonance with the same H-band EMIC wave at the same low latitude $\lambda < 10°$, combining the resonance condition with the dispersion relation of EMIC waves shows that $p \cdot \cos \alpha_{eq}$ is nearly an invariant (Mourenas et al., 2016). This finally gives:

$$\frac{D_{\alpha\alpha}(E_{GPS}, \alpha_{eq,GPS})}{D_{\alpha\alpha}(E_{ELFIN}, \alpha_{eq,LC})} \approx \frac{(1 + 2E_{ELFIN})\left(E_{GPS}^2 + E_{GPS}\right)^{1/2}}{(1 + 2E_{GPS})\left(E_{ELFIN}^2 + E_{ELFIN}\right)^{1/2}}, \tag{1}$$

where E_{ELFIN} is given by

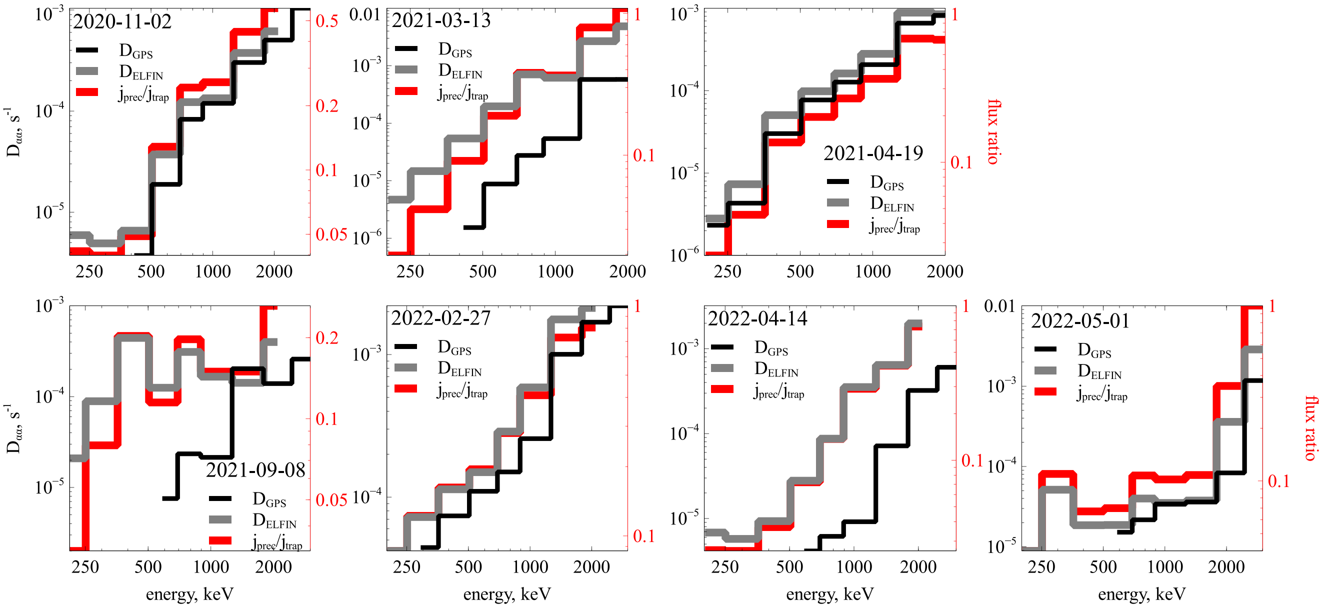

Figure 2. For the seven events listed in Table 1, the ratio j_{prec}/j_{trap} of net precipitating to trapped electron flux measured at low altitude by ELFIN CubeSats is displayed as a function of energy (in red), averaged over $\sim 15-30$ spacecraft spins (i.e., 45–90 s), using data well above instrument noise level (>5 counts/s). The pitch-angle diffusion rate $D_{\alpha\alpha}(\alpha_{eq,LC}, E_{ELFIN})$ of electrons near the loss cone angle $\alpha_{eq,LC}$ by H-band EMIC waves, inferred from j_{prec}/j_{trap} measured at ELFIN using quasi-linear diffusion theory, is also shown for each event (in gray), as well as the corresponding pitch-angle diffusion rate $D_{\alpha\alpha}(\alpha_{eq,GPS}, E_{GPS})$ of electrons of higher equatorial pitch-angles $\alpha_{eq,GPS}$ and higher energy E_{GPS} scattered by the same H-band EMIC waves on the same geomagnetic field line (in black). Such electrons are detected by Global Positioning System spacecraft during the same events on the same geomagnetic field line, and their diffusion rate $D_{\alpha\alpha}(\alpha_{eq,GPS}, E_{GPS})$ is inferred from the displayed $D_{\alpha\alpha}(\alpha_{eq,LC}, E_{ELFIN})$ using Equations 1 and 2, as long as j_{prec}/j_{trap} does not start to increase toward lower energy.

$$E_{ELFIN} \approx \left(\frac{1}{4} + \frac{\cos^2 \alpha_{eq,GPS}}{\cos^2 \alpha_{eq,LC}}\left(E_{GPS}^2 + E_{GPS}\right)\right)^{1/2} - \frac{1}{2}. \tag{2}$$

The needed $D_{\alpha\alpha}(E_{ELFIN}, \alpha_{eq,LC})$ in Equation 1 is obtained by interpolation between the two $D_{\alpha\alpha}(E_{ELFIN,i}, \alpha_{eq,LC})$ values directly inferred from ELFIN data (Mourenas et al., 2023, 2024) in the two energy channels $E_{ELFIN,i}$ closest to E_{ELFIN}. Note that energy, E, in Equations 1 and 2 and throughout the text, is in MeV. Since ELFIN energy channels have a full width $\Delta E/E \approx 40\%$ (Angelopoulos et al., 2020, 2023), this procedure naturally accommodates errors smaller than $\sim 20\%$ in the value of E_{ELFIN} inferred using the approximate Equation 2.

The precipitating to trapped electron flux ratio, j_{prec}/j_{trap}, measured by ELFIN CubeSats during each event over 20–60 s (Angelopoulos et al., 2023; Mourenas et al., 2021), is displayed (in red) in Figure 2 as a function of electron energy. Here, j_{prec} denotes the net precipitating flux, calculated by subtracting the upward flux from the downward flux measured at ELFIN inside the local bounce loss cone—the upward flux serving as a proxy for the electron flux backscattered into the loss cone by the atmosphere on the opposite end of the same geomagnetic field line (Mourenas et al., 2021). The corresponding $D_{\alpha\alpha}(\alpha_{eq,LC}, E_{ELFIN})$ is also displayed (in gray). It is inferred from j_{prec}/j_{trap}, assuming a quasi-equilibrium PAD after minutes to hours of wave-particle interactions, using the approximate relationship $z_0 \simeq \left(10^4 + 260\, j_{trap}/j_{prec}\right)^{1/2} - 100$ valid to within $\sim 25\%$ when $j_{prec}/j_{trap} < 0.87$ (Mourenas et al., 2023, 2024), with $z_0 = 2\alpha_{eq,LC}/\left(D_{\alpha\alpha}[\alpha_{eq,LC}]\tau_B\right)^{1/2}$ and τ_B the electron bounce period (Schulz & Lanzerotti, 1974). The high levels of $j_{prec}/j_{trap} \approx 0.1-0.5$ and $D_{\alpha\alpha}(\alpha_{eq,LC}, E_{ELFIN}) > 10^{-4}$ s^{-1} at $E_{ELFIN} \sim 0.6-1$ MeV in Figure 2 strongly suggest that such EMIC wave-driven electron precipitation is occurring in a plasmaspheric plume, with a high plasma frequency to gyrofrequency ratio $f_{pe}/f_{ce} > 15$, because a lower f_{pe}/f_{ce} would require a high EMIC wave power unrealistically close to the proton gyrofrequency (X. Shi et al., 2024; Summers & Thorne, 2003; X.-J. Zhang, Li, Thorne, et al., 2016). Plasmaspheric plumes are indeed often observed in the noon-dusk sector during the main and recovery phases of storms (Darrouzet et al., 2009; Moldwin et al., 2004), the place and time of all ELFIN observations in Table 1.

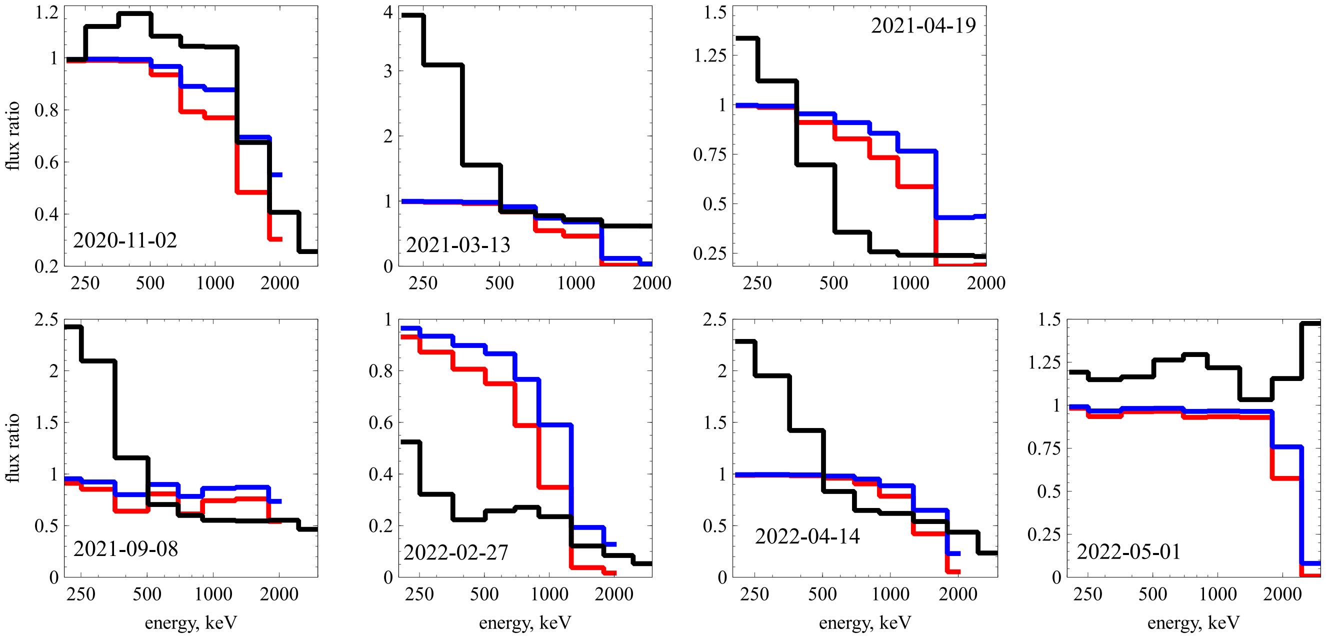

Figure 3. Electron flux decrease j_{t2}/j_{t1} (in black) observed by Global Positioning System spacecraft (i.e., ratio of the flux j_{t2} measured during the 2 hr following ELFIN observations to the flux j_{t1} averaged between -12 and -4 hr before ELFIN observations), as a function of energy E during the seven events in Table 1. The corresponding flux decrease $(j_{t2}/j_{t1})_{EMIC}(\Delta t)$ produced by EMIC wave-driven electron precipitation into the atmosphere (over 4 hr in MLT) is also shown for EMIC waves present over a period of $\Delta t = 1$ hr (in blue) or of $\Delta t = 2$ hr (in red).

The diffusion rate $D_{\alpha\alpha}(E_{GPS}, \alpha_{eq,GPS})$ of electrons at GPS spacecraft (scattered by the same H-band EMIC waves as electrons of lower energy and lower α_{eq} measured by ELFIN on the same field line) is inferred from $D_{\alpha\alpha}(\alpha_{eq,LC}, E_{ELFIN})$ using Equations 1 and 2 and displayed in Figure 2 (in black). If a minimum of j_{prec}/j_{trap} exists at low to medium energy E_{ELFIN}, $D_{\alpha\alpha}(E_{GPS}, \alpha_{eq,GPS})$ is calculated only above this minimum, because electron precipitation at lower energy is likely due to whistler-mode waves and not to EMIC waves (Angelopoulos et al., 2023). Figure 2 shows that at a given energy, $D_{\alpha\alpha}(E_{GPS}, \alpha_{eq,GPS})$ (in black) is smaller than $D_{\alpha\alpha}(\alpha_{eq,LC}, E_{ELFIN})$ (in gray) and that this reduction is more important for a higher $\alpha_{eq,GPS}$, because cyclotron resonance with electrons of higher $\alpha_{eq,GPS}$ occurs with higher frequency H-band EMIC waves, of lower intensity (Angelopoulos et al., 2023; X. Shi et al., 2024). In fact, Equation 2 shows that cyclotron resonance of electrons at $\alpha_{eq,GPS} > \alpha_{eq,LC}$ with the same wave as electrons at $(\alpha_{eq,LC}, E_{ELFIN})$ occurs at a higher energy $E_{GPS} > E_{ELFIN}$ and that the ratio E_{GPS}/E_{ELFIN} increases with $\alpha_{eq,GPS}$. The corresponding energy shift $\Delta E = E_{GPS} - E_{ELFIN}$ is larger for a higher $\alpha_{eq,GPS}$, as during the 2021-09-08, 2021-03-13, and 2022-04-14 events, resulting in a large positive energy shift, by ΔE, of the black curve showing $D_{\alpha\alpha}(E_{GPS}, \alpha_{eq,GPS})$ compared with the gray curve showing $D_{\alpha\alpha}(E_{ELFIN}, \alpha_{eq,LC})$. The main difference between $D_{\alpha\alpha}(E_{GPS}, \alpha_{eq,GPS})$ and $D_{\alpha\alpha}(E_{ELFIN}, \alpha_{eq,LC})$ in Figure 2 is due to this energy shift, with an additional multiplicative factor provided on the right-hand-side of Equation 1.

2.4. Can EMIC Wave-Driven Electron Precipitation Explain Dropouts Measured by GPS Spacecraft?

Next, the drop in electron flux measured by GPS spacecraft during the 7 events in Table 1 is compared in Figure 3 with an estimate of the drop in electron flux produced by EMIC wave-driven electron precipitation alone, which can be derived from diffusion rates displayed in Figure 2. The drop in electron flux at GPS spacecraft is calculated as the ratio j_{t2}/j_{t1} of the flux $j_{t2}(E)$ measured during the 2 hr following ELFIN observations of EMIC wave-driven MeV electron precipitation to the flux $j_{t1}(E)$ averaged between -12 and -4 hr before such ELFIN observations.

During the events in Table 1, the presence of intense H-band EMIC waves has been deduced from the strong $1-2$ MeV electron precipitation measured by ELFIN CubeSats. Such intense EMIC waves in the noon-dusk sector, probably mainly driven by magnetosphere compression at times of enhanced solar wind dynamic pressure P_{dyn}, have a typical duration $\Delta t \approx 1-2$ hr (Angelopoulos et al., 2023; Blum et al., 2017, 2020; Usanova et al., 2008). Accordingly, the drop in electron flux produced by EMIC wave-driven pitch-angle diffusion toward the loss cone can be estimated over this typical duration $\Delta t \approx 1-2$ hr, based on the diffusion rates $D_{\alpha\alpha}(\alpha_{eq})$ inferred from ELFIN measurements in Figure 2. A useful analytical estimate of the corresponding lifetime τ_L of electrons at $(E_{GPS}, \alpha_{eq,GPS})$ has been derived by Albert and Shprits (2009). It can be approximately rewritten as a function of $D_{\alpha\alpha}(\alpha_{eq,LC}, E_{ELFIN})$ and $D_{\alpha\alpha}(E_{GPS}, \alpha_{eq,GPS})$ values provided in Figure 2, giving:

$$\tau_L(\alpha_{eq,GPS}) \approx \frac{\ln(\sin\alpha_{eq,GPS}/\sin\alpha_{eq,LC})}{4\,D_{\alpha\alpha}(\alpha_{eq,LC})}\left(1+\frac{\tan\alpha_{eq,LC}\,D_{\alpha\alpha}(\alpha_{eq,LC})}{\tan\alpha_{eq,GPS}\,D_{\alpha\alpha}(\alpha_{eq,GPS})}\right), \tag{3}$$

where τ_L and $D_{\alpha\alpha}$ are taken at the same energy E. Assuming a realistic scaling of the form $D_{\alpha\alpha} = (\cos\alpha_{eq}/\cos\alpha_{eq,LC})^A\,D_{\alpha\alpha}(\alpha_{eq,LC})$, consistent with the more and more rapid decrease of resonant EMIC wave power at frequencies higher than the frequency of peak power in EMIC wave statistics (Angelopoulos et al., 2023; X. Shi et al., 2024), we checked that τ_L given by Equation 3 recovers numerically calculated lifetimes (Albert & Shprits, 2009) within a factor of ~ 1.5 when $(\tan\alpha_{eq,LC}\,D_{\alpha\alpha}(\alpha_{eq,LC}))/(\tan\alpha_{eq,GPS}\,D_{\alpha\alpha}(\alpha_{eq,GPS}))$ varies between 0.03 and 8, as for typical parameters in Figure 2.

It is reasonable to assume that intense EMIC wave-driven precipitation is present over only ≈ 4 hr in MLT (i.e., over $\sim 1/6$ of the azimuthal drift period of electrons), in agreement with statistical EMIC wave observations (Blum et al., 2017; Kersten et al., 2014; Ross et al., 2021) and EMIC wave-driven precipitation events (Capannolo et al., 2019, 2021; Shekhar et al., 2017). After a burst of $\Delta t \approx 1-2$ hr of electron pitch-angle scattering by EMIC waves toward the loss cone, the decrease of electron flux at $\alpha_{eq} \sim \alpha_{eq,GPS}$ should therefore correspond to a final to initial flux ratio

$$\left(\frac{j_{t2}}{j_{t1}}\right)_{EMIC} \approx \exp\left(\frac{-\Delta t}{6\,\tau_L(E,\alpha_{eq,GPS})}\right), \tag{4}$$

with $\tau_L(E, \alpha_{eq,GPS})$ given by Equation 3 based on ELFIN measurements alone.

Most EMIC-wave-driven pitch-angle diffusion rates displayed in Figure 2 are at least three orders of magnitude larger than typical MLT-averaged diffusion rates due to whistler-mode hiss or chorus waves at the same L-shells and α_{eq} for $E \sim 1-3$ MeV (Agapitov et al., 2018; Li et al., 2015, 2019), and also much larger than typical local diffusion rates due to plume hiss (Li et al., 2019). Therefore, the dominant time-averaged and MLT-averaged pitch angle diffusion of $\sim 1-3$ MeV electrons at $\alpha_{eq} \leq \alpha_{eq,GPS}$ is likely due to EMIC waves over the several hours, near the time of ELFIN observations, during which the electron flux dropout occurs. During that period, $(j_{t2}/j_{t1})_{EMIC}$ given by Equation 4 should provide a good estimate of the drop of $\sim 1-3$ MeV electron flux due to precipitation by all the waves present at the same L in all MLT sectors.

Figure 3 provides a comparison between the flux decrease j_{t2}/j_{t1} observed by GPS spacecraft (in black) and the expected flux decrease $(j_{t2}/j_{t1})_{EMIC}(\Delta t)$ due to EMIC wave-driven precipitation lasting $\Delta t = 1$ hour (in blue) to $\Delta t = 2$ hours (in red), given by Equation 4, for each of the 7 events provided in Table 1, using $\tau_L = +\infty$ when $D_{\alpha\alpha}(\alpha_{eq,GPS})$ is null or unavailable.

Figure 3 shows that, during the six events exhibiting electron flux dropouts, EMIC wave-driven electron precipitation alone can account for a significant fraction of the observed flux decrease from 1.5 MeV to $2-3$ MeV for $\Delta t = 1$ hr, and can explain the full magnitude of this observed flux decrease for $\Delta t = 2$ hr during five of these six events. These results demonstrate that EMIC wave-driven electron precipitation can potentially control the magnitude of electron flux dropouts at $\sim 1.5-3.0$ MeV.

In addition, during two of the five events with dropouts down to ~ 0.5 MeV, on 2021-03-13 and 2021-09-08, EMIC wave-driven electron precipitation alone can account for most of the observed flux drop from ~ 0.5 MeV up to $2-3$ MeV. During four events, it can lead to a 20% flux drop at ~ 0.6 MeV. This suggests that EMIC wave-driven electron precipitation can sometimes modulate the dropout magnitude down to unexpectedly low energy (~ 0.5 MeV).

Note that the estimate $(j_{t2}/j_{t1})_{EMIC}$ of the EMIC wave-driven electron flux reduction, inferred from ELFIN measurements, relies on the important assumption that the same H-band EMIC waves, which likely drove the electron precipitation measured by ELFIN during $\approx 20-60$ seconds, remained present during $\Delta t\approx 1-2$ hr over ≈ 4 hr in MLT with a similar MLT-averaged and time-averaged wave power distribution in frequency as during ELFIN observations. An actual MLT-averaged and time-averaged wave power smaller (higher) at high frequencies than during ELFIN measurements would lead to a weaker (stronger) flux reduction at low energy than in Figure 3, and a smaller (higher) MLT-averaged and time-averaged wave power at low frequencies would lead to a weaker (stronger) flux reduction at high energy. In particular, a decrease of the MLT range where EMIC waves are assumed to be present by a factor of 2 would be equivalent to a similar decrease of the assumed duration Δt of these waves. The present estimate $\left(j_{t2}/j_{t1}\right)_{EMIC}$ also relies on the assumption that the electron plasma frequency to gyrofrequency ratio remained approximately the same as during ELFIN observations over the ≈ 4 hours in MLT where the waves are assumed to be present. A significantly lower plasma density would indeed prevent an efficient precipitation of low energy electrons (Mourenas et al., 2016; Summers & Thorne, 2003). Finally, Equation 3 is valid for a MLT-averaged and time-averaged H-band EMIC wave power monotonically decreasing from the peak power frequency toward higher frequencies, as expected based on EMIC wave statistics from the Van Allen Probes (X. Shi et al., 2024). The above assumptions allow us to infer $\left(j_{t2}/j_{t1}\right)_{EMIC}$ from ELFIN measurements of the precipitating-to-trapped flux ratio at various energies, because each $D_{\alpha\alpha}(\alpha_{eq,LC})$ inferred from such measurements inherently contains all the information about the resonant wave power, plasma frequency to gyrofrequency ratio, and ion composition (Angelopoulos et al., 2023).

During six of the seven events in Figure 3, there is a simultaneous increase of electron flux below $300-500$ keV, which likely corresponds to significant electron injections. Note that such injections may mask potential electron losses due to EMIC waves in this low energy range.

During the remaining 2022-05-01 event, with no observed dropout, the estimated EMIC wave-driven electron loss is negligible below 2 MeV in agreement with observations, but it becomes significant at 2–3 MeV contrary to observations. The electron flux measured by GPS spacecraft actually increases at all energies during this event, but more at 3 MeV than at lower energies. This suggests the presence of both electron injections below 500 keV and significant chorus wave-driven electron acceleration in the dawn sector, where the minimum plasmapause position is lower than the examined L-shell (see Table 1).

Previous works have indeed shown that in the presence of both EMIC wave-driven electron precipitation (in a noon-dusk plume) and chorus wave-driven electron acceleration (in the dawnside trough), the electron flux $j(E)$ at $\alpha_{eq}\geq 45^\circ$ should rapidly tend toward a steady-state shape, $j_{st}(E)$, which represents an attractor for the system dynamics (Hua et al., 2022; Mourenas et al., 2022, 2023). Therefore, the initial gradient $\partial j(E)/\partial E$ should control the flux evolution over the next hours (Mourenas et al., 2022). If the initial flux decreases slower toward higher energy than the steady-state shape $j_{st}(E)$, the flux will drop at high E to assume this steady-state shape (Mourenas et al., 2016), but if the initial flux decreases faster than $j_{st}(E)$ the flux will instead increase at high E to assume this shape (Mourenas et al., 2022, 2023).

Accordingly, it is important to examine the evolution of the electron flux at $\sim 1-2$ MeV in the presence of both EMIC and chorus waves (in different MLT sectors) during the events in Table 1, to check whether chorus wave-driven electron acceleration could have partly counterbalanced EMIC wave-driven electron loss. Using the fair approximation $E(E+1)\simeq(E+1/2)^2$ for E in MeV, the chorus wave-driven electron energization rate, D_{EE}, is nearly independent of E in this energy range for quasi-parallel waves (Mourenas et al., 2012). Assuming that the effective time-averaged electron lifetime $\tau_{L,eff}$ is roughly constant in this energy range, the steady-state solution to the Fokker-Planck equation (Horne et al., 2005) describing the evolution of the electron distribution function at $\alpha_{eq}>30^\circ$ corresponds to a steady-state flux $j_{st}(E)$ given by (Mourenas et al., 2014, 2022):

$$\frac{j_{st}(E)}{j_{st}(1\text{ MeV})}\simeq E\cdot\exp\left(-\frac{(E-1)}{\sqrt{\tau_{L,eff}\,D_{EE}}}\right),\tag{5}$$

for $E\in[1,2]$ MeV, with $D_{EE}\simeq 2\,B_w^2 f_{ce}^{3/2} f^{1/2}/f_{pe}^3$ hour^{-1}, where B_w^2 (in pT^2) is the MLT-averaged chorus wave power at magnetic latitudes $\lambda\leq 10^\circ$, f is the wave frequency, f_{pe} the plasma frequency, and f_{ce} the equatorial gyrofrequency (Agapitov et al., 2019). For typical parameters at $L\approx 4.5-6.5$ during active periods with $Kp\approx 5$ favoring electron acceleration ($B_w^2\sim 100^2$ pT^2, $f_{pe}/f_{ce}\sim 4$, and $f/f_{ce}\sim 0.25$), we get $D_{EE}\simeq 6\cdot 10^{-5}\times L^3$ hour^{-1}

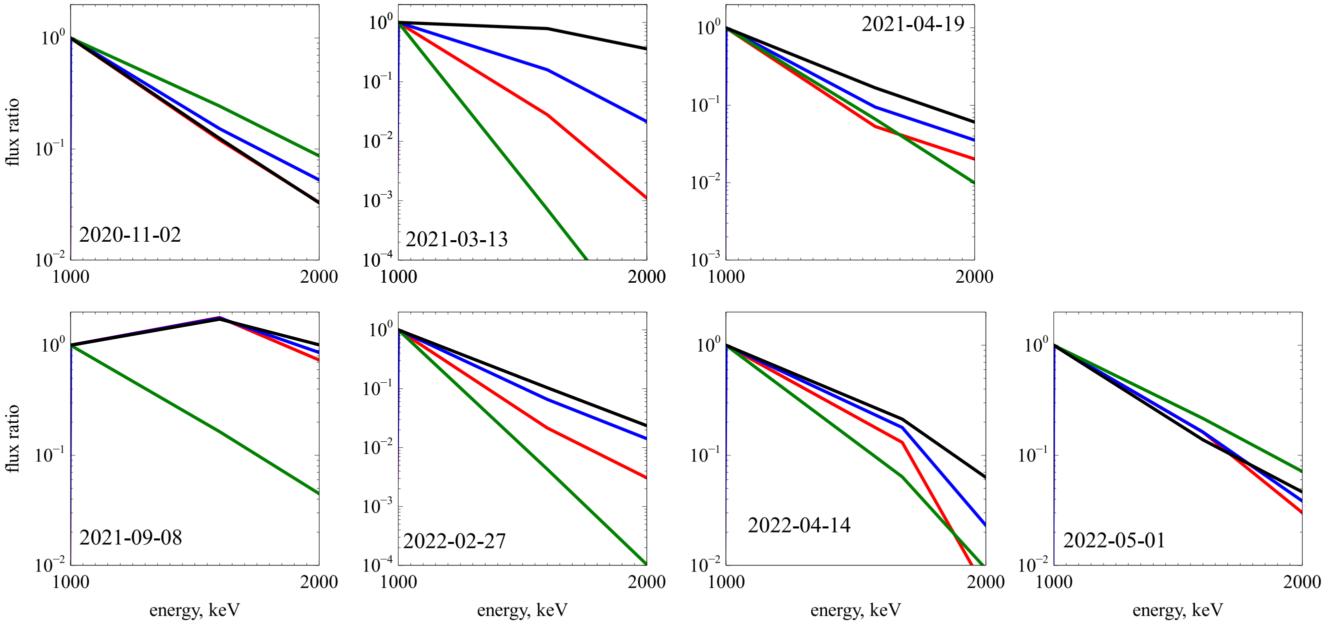

Figure 4. Final normalized differential electron flux $j_{t2}(E)/j_{t2}(1\text{ MeV})$ measured by Global Positioning System spacecraft (black), final normalized differential electron flux due to EMIC wave-driven loss alone $\left((j_{t2}/j_{t1})_{EMIC}\cdot j_{t1}\right)_E/\left((j_{t2}/j_{t1})_{EMIC}\cdot j_{t1}\right)_{1\text{ MeV}}$ for $\Delta t = 1$ hr (blue) and $\Delta t = 2$ hr (red), and steady-state attractor normalized differential electron flux $j_{st}(E)/j_{st}(1\text{ MeV})$ (green), as a function of E during all events.

(Agapitov et al., 2018, 2019; Wong et al., 2024). Since a dropout of electron flux takes $\sim 2-4$ hr and intense noon-dusk EMIC waves due to magnetosphere compression typically last $\Delta t \sim 1-2$ hr, EMIC waves are assumed to be present half of the time during a dropout, over 4 hr in MLT, giving an effective lifetime $\tau_{L,eff} \simeq 12\ \tau_L(1.5\text{ MeV})$ at $1-2$ MeV, with τ_L given by Equation 3.

Figure 4 shows the final normalized electron flux $j_{t2}(E)/j_{t2}(1\text{ MeV})$ measured by GPS spacecraft (black), the final normalized flux due to EMIC wave-driven loss alone $\left((j_{t2}/j_{t1})_{EMIC}\cdot j_{t1}\right)_E/\left((j_{t2}/j_{t1})_{EMIC}\cdot j_{t1}\right)_{1\text{ MeV}}$ for $\Delta t = 1$ hr (blue) and $\Delta t = 2$ hr (red), and the steady-state normalized flux $j_{st}(E)/j_{st}(1\text{ MeV})$ (green) estimated using Equation 5, during all events in Table 1. It is worth noting, however, that the steady-state normalized flux $j_{st}(E)/j_{st}(1\text{ MeV})$ given by Equation 5 is strictly valid, in principle, only for $\alpha_{eq,GPS} > 30°$, because the actual ratio $j(2\text{ MeV})/j(1\text{ MeV})$ can strongly decrease at $\alpha_{eq} < 30°$ in the presence of strong chorus wave-driven electron energy diffusion, while it usually remains roughly constant at $\alpha_{eq} > 30°$ (Li et al., 2014).

Figure 4 shows that during five of the six events with observed dropouts in Table 1 both the final normalized flux measured by GPS spacecraft (black) and the final normalized fluxes due to EMIC wave-driven loss alone (blue and red) are less steeply decreasing toward higher energy than the normalized flux of the steady-state attractor (green), or are decreasing roughly similarly to the normalized flux of the steady-state attractor (as for $\Delta t = 2$ hr during the 2022-04-14 event). This means that five of these six dropouts of $1.5-2$ MeV electron flux measured by GPS spacecraft can really be produced by EMIC waves alone, even in the presence of strong chorus wave-driven electron acceleration, due to the very fast losses. The exception is the 2020-11-02 dropout event. This particular event corresponds to the lowest $\alpha_{eq,GPS}$ value (22°) in Table 1. As noted above, the actual ratio $j(2\text{ MeV})/j(1\text{ MeV})$ may strongly decrease at such low $\alpha_{eq} < 30°$ in the presence of chorus wave-driven electron energy diffusion compared to the steady-state ratio $j_{st}(2\text{ MeV})/j_{st}(1\text{ MeV})$ estimated for $\alpha_{eq} > 30°$ in Equation 5, potentially by up to a factor of $\approx 3-5$ (Li et al., 2014), which could decrease the normalized flux of the steady-state attractor (green) at 2 MeV below the final normalized flux measured by GPS spacecraft (black) during the 2020-11-02 event in Figure 4. Moreover, the extremely low $Kp = 0.0-0.7$ over the 12 hr preceding ELFIN observations on 2020-11-02 suggests the presence of only very weak chorus wave power, which would rule out significant electron energy diffusion and exclude the existence of a steady-state attractor $j_{st}(E)$ during this event. The only other event with $\alpha_{eq,GPS} < 30°$ is the 2021-04-19 event, with $\alpha_{eq,GPS} = 25°$, for which the normalized flux of the steady-state attractor at 2 MeV (green) may also be overestimated in Figure 4.

The estimated final flux (blue) is also in good agreement with measurements (black) during the 2021-04-19, 2021-09-08, 2022-02-27, and 2022-04-14 events in Figure 4. This good agreement is especially noticeable for the 2022-02-27 and 2022-04-14 events exhibiting a strong flux drop at $1.5-2$ MeV compared to 1 MeV, and it is then due to the good agreement, in Figure 3, between the measured flux decrease at $1-2$ MeV and the expected flux decrease due to EMIC waves. During the 2021-04-19 and 2021-09-08 events, as the measured flux decreases by a similar fraction at 1 MeV and at $1.5-2$ MeV, the final measured $j_{t2}(E)/j_{t2}(1\text{ MeV})$ remains the same as the initial $j_{t1}(E)/j_{t1}(1\text{ MeV})$ and it also remains close to the estimated flux ratio when including the weak EMIC wave effects found in Figure 3 during these two events. On 2021-03-13, the measured final flux (black) is less steeply decreasing than the estimated final flux (blue) in Figure 4. This suggests that the most intense EMIC waves in cyclotron resonance with 2 MeV electrons during this event may have been four times more short-lived than the weaker waves in resonance with 1 MeV electrons.

During the 2022-05-01 event, the final measured flux (black) is slightly more steeply decreasing toward higher energy at $1-2$ MeV than the steady-state attractor shape (green), although close to the estimated final flux due to EMIC waves alone (blue). In such a case, chorus wave-driven electron acceleration may have prevented an EMIC wave-driven electron flux drop and instead produced the slight increase of $1.5-2$ MeV electron flux observed during this event (see Figure 3).

During the 2020-11-02 and 2022-04-14 events, the precipitating-to-trapped electron flux ratio j_{prec}/j_{trap} reaches a minimum at 300 keV in Figure 2. Since the strong EMIC wave-driven electron precipitation at $E \leq 1$ MeV suggests that these events took place inside a plasmaspheric plume, this minimum of j_{prec}/j_{trap} could be due to the simultaneous presence of whistler-mode hiss waves (Su et al., 2018; W. Zhang et al., 2019). Such hiss waves can indeed provide stronger electron pitch-angle scattering toward the loss cone at 100–200 keV than at higher energy at $L > 4$ (Li et al., 2015, 2019; Ma et al., 2021; Mourenas et al., 2017). Contrary to higher frequency chorus waves, hiss waves are inefficient at energizing electrons (Kennel & Petschek, 1966; Mourenas et al., 2023). Therefore, a combination of EMIC and hiss wave-driven diffusion can easily lead to dropouts of whole electron populations up to high equatorial pitch-angles (Mourenas et al., 2016).

3. Conclusions

The effects of EMIC waves on the dynamics of trapped electron fluxes in the Earth's outer radiation belt has long been a topic of intense research. However, the contribution of EMIC wave-driven electron losses to rapid dropouts of electron flux recorded during disturbed periods has not yet been determined. In the present paper, contemporaneous measurements, on the same L-shell, of trapped electron flux at 20,000 km altitude by GPS spacecraft and of trapped and precipitating electron fluxes at 450 km altitude by ELFIN CubeSats, have been used for investigating the contribution of EMIC wave-driven electron precipitation to electron flux dropouts recorded well below the LCDS of trapped electrons, where electron loss due to magnetopause shadowing may not explain the full magnitude of dropouts.

During six of the seven selected events, the strong 1–2 MeV EMIC wave-driven electron precipitation detected in the noon-dusk sector at low altitude by ELFIN takes place within 1–2 hr of a dropout of relativistic electron flux recorded at high altitude by GPS spacecraft. Quasi-linear diffusion theory has been used to infer EMIC wave-driven electron pitch angle diffusion rates from ELFIN measurements of precipitating and trapped electron fluxes during these events. Such inferred pitch angle diffusion rates allowed us to provide quantitative estimates of the electron flux drop due to EMIC wave-driven precipitation alone, based on the typical spatial and temporal scales of EMIC waves.

During all events, we showed that EMIC wave-driven electron precipitation alone may have been sufficient to account for the full magnitude of the observed dropout at 1.5–3 MeV. During 40% of the events with dropouts extending to low energy, we found that a fraction of electron losses at $0.5-1$ MeV may sometimes be also due to scattering by EMIC waves, together with outward radial diffusion toward the LCDS. In addition, we showed that the contemporaneous presence of chorus wave-driven electron acceleration in a low density region in the dawn sector cannot have counterbalanced EMIC wave-driven electron loss in a noon-dusk sector plume during events with observed strong dropouts, but that it might explain why a flux increase was observed instead of a flux drop during another event. The present results therefore suggest that EMIC wave-driven electron precipitation may often modulate dropout magnitude above 1 MeV in the heart of the outer radiation belt.

Comprehensive spacecraft statistics of the spatial and temporal extents of EMIC waves will be needed in the future to obtain more precise estimates of their impact on dropouts, especially below 1 MeV. The applicability of quasi-linear diffusion theory for describing electron transport toward the loss cone through interactions with EMIC waves should also be examined in more detail.

Data Availability Statement

Electron fluxes measured by ELFIN are available in CDF format (ELFIN, 2024). Los Alamos National Laboratory CXD data of electron flux from GPS spacecraft are available from NOAA (GPS, 2024). The LANL* code is freely available (LANL* CODE, 2024). OMNI data of $Sym - H$, Kp, IMF B_z, and $Pdyn$ are available from the Kyoto World Data Center for Geomagnetism (WDC FOR GEOMAGNETISM, 2024). The data was retrieved and analyzed using PySPEDAS and SPEDAS, see Angelopoulos et al. (2019).

Acknowledgments
A.V.A., X.J.Z., and V.A. acknowledge support by NASA awards 80NSSC20K1270, 80NSSC23K0403, 80NSSC24K0558, and NSF Grants AGS-1242918, AGS-2019950, and AGS-2021749. We are grateful to NASA's CubeSat Launch Initiative for ELFIN's successful launch in the desired orbits. We acknowledge early support of ELFIN project by the AFOSR, under its University Nanosat Program, UNP-8 project, contract FA9453-12-D-0285, and by the California Space Grant program. We sincerely acknowledge critical contributions of numerous volunteer ELFIN team student members.

References

Agapitov, O. V., Mourenas, D., Artemyev, A., Hospodarsky, G., & Bonnell, J. W. (2019). Time scales for electron quasi-linear diffusion by lower-band chorus waves: The effects of ω_{pe}/Ω_{ce} dependence on geomagnetic activity. *Geophysical Research Letters*, *46*(12), 6178–6187. https://doi.org/10.1029/2019GL083446

Agapitov, O. V., Mourenas, D., Artemyev, A. V., Mozer, F. S., Hospodarsky, G., Bonnell, J., & Krasnoselskikh, V. (2018). Synthetic empirical chorus wave model from combined Van Allen Probes and Cluster statistics. *Journal of Geophysical Research: Space Physics*, *123*(1), 297–314. https://doi.org/10.1002/2017JA024843

Albert, J.-M., Selesnick, R. S., Morley, S. K., Henderson, M. G., & Kellerman, A. C. (2018). Calculation of last closed drift shells for the 2013 GEM radiation belt challenge events. *Journal of Geophysical Research: Space Physics*, *123*(11), 9597–9611. https://doi.org/10.1029/2018JA025991

Albert, J. M., & Shprits, Y. Y. (2009). Estimates of lifetimes against pitch angle diffusion. *Journal of Atmospheric and Solar-Terrestrial Physics*, *71*(16), 1647–1652. https://doi.org/10.1016/j.jastp.2008.07.004

An, X., Artemyev, A., Angelopoulos, V., Zhang, X.-J., Mourenas, D., Bortnik, J., & Shi, X. (2024). Nonresonant scattering of energetic electrons by electromagnetic ion cyclotron waves: Spacecraft observations and theoretical framework. *Journal of Geophysical Research: Space Physics*, *129*(3), e2023JA031863. https://doi.org/10.1029/2023JA031863

Angelopoulos, V., Cruce, P., Drozdov, A., Grimes, E. W., Hatzigeorgiu, N., King, D. A., et al. (2019). The Space Physics Environment Data Analysis System (SPEDAS). *Space Science Reviews*, *215*(1), 9. https://doi.org/10.1007/s11214-018-0576-4

Angelopoulos, V., Tsai, E., Bingley, L., Shaffer, C., Turner, D. L., Runov, A., et al. (2020). The ELFIN Mission. *Space Science Reviews*, *216*(5), 103. https://doi.org/10.1007/s11214-020-00721-7

Angelopoulos, V., Zhang, X. J., Artemyev, A. V., Mourenas, D., Tsai, E., Wilkins, C., et al. (2023). Energetic electron precipitation driven by electromagnetic ion cyclotron waves from ELFIN's low altitude perspective. *Space Science Reviews*, *219*(5), 37. https://doi.org/10.1007/s11214-023-00984-w

Artemyev, A. V., Mourenas, D., Zhang, X. J., & Vainchtein, D. (2022). On the incorporation of nonlinear resonant wave-particle interactions into radiation belt models. *Journal of Geophysical Research: Space Physics*, *127*(9), e30853. https://doi.org/10.1029/2022JA030853

Blum, L. W., Bonnell, J. W., Agapitov, O., Paulson, K., & Kletzing, C. (2017). EMIC wave scale size in the inner magnetosphere: Observations from the dual Van Allen Probes. *Geophysical Research Letters*, *44*(3), 1227–1233. https://doi.org/10.1002/2016GL072316

Blum, L. W., Halford, A., Millan, R., Bonnell, J. W., Goldstein, J., Usanova, M., et al. (2015). Observations of coincident EMIC wave activity and duskside energetic electron precipitation on 18–19 January 2013. *Geophysical Research Letters*, *42*(14), 5727–5735. https://doi.org/10.1002/2015GL065245

Blum, L. W., Remya, B., Denton, M. H., & Schiller, Q. (2020). Persistent EMIC wave activity across the nightside inner magnetosphere. *Geophysical Research Letters*, *47*(6), e87009. https://doi.org/10.1029/2020GL087009

Boynton, R. J., Mourenas, D., & Balikhin, M. A. (2016). Electron flux dropouts at Geostationary Earth Orbit: Occurrences, magnitudes, and main driving factors. *Journal of Geophysical Research: Space Physics*, *121*(9), 8448–8461. https://doi.org/10.1002/2016JA022916

Boynton, R. J., Mourenas, D., & Balikhin, M. A. (2017). Electron flux dropouts at $L \sim 4.2$ from global positioning system satellites: Occurrences, magnitudes, and main driving factors. *Journal of Geophysical Research: Space Physics*, *122*, 11. https://doi.org/10.1002/2017JA024523

Bruno, A., Blum, L. W., de Nolfo, G. A., Kataoka, R., Torii, S., Greeley, A. D., et al. (2022). EMIC-wave driven electron precipitation observed by CALET on the International Space Station. *Geophysical Research Letters*, *49*(6), e2021GL097529. https://doi.org/10.1029/2021GL097529

Cao, J., Shprits, Y. Y., Ni, B., & Zhelavskaya, I. S. (2017). Scattering of ultra-relativistic electrons in the Van Allen radiation belts accounting for hot plasma effects. *Scientific Reports*, *7*(1), 17719. https://doi.org/10.1038/s41598-017-17739-7

Capannolo, L., Li, W., Ma, Q., Shen, X. C., Zhang, X. J., Redmon, R. J., et al. (2019). Energetic electron precipitation: Multievent analysis of its spatial extent during EMIC wave activity. *Journal of Geophysical Research: Space Physics*, *124*(4), 2466–2483. https://doi.org/10.1029/2018JA026291

Capannolo, L., Li, W., Spence, H., Johnson, A. T., Shumko, M., Sample, D., & Klumpar, J. (2021). Energetic electron precipitation observed by FIREBIRD-II potentially driven by EMIC waves: Location, extent, and energy range from a multievent analysis. *Geophysical Research Letters*, *48*(5), e2020GL091564. https://doi.org/10.1029/2023GL103519

Chen, H., Gao, X., Lu, Q., Tsurutani, B. T., & Wang, S. (2020). Statistical evidence for EMIC wave excitation driven by substorm injection and enhanced solar wind pressure in the Earth's magnetosphere: Two different EMIC wave sources. *Geophysical Research Letters*, *47*(21), e2020GL090275. https://doi.org/10.1029/2020GL090275

Chen, H., Gao, X., Lu, Q., & Wang, S. (2019). Analyzing EMIC waves in the inner magnetosphere using long-term Van Allen Probes observations. *Journal of Geophysical Research: Space Physics*, *124*(9), 7402–7412. https://doi.org/10.1029/2019JA026965

Chen, L., Thorne, R. M., Shprits, Y., & Ni, B. (2013). An improved dispersion relation for parallel propagating electromagnetic waves in warm plasmas: Application to electron scattering. *Journal of Geophysical Research: Space Physics*, *118*(5), 2185–2195. https://doi.org/10.1002/jgra.50260

Darrouzet, F., Gallagher, D. L., André, N., Carpenter, D. L., Dandouras, I., Décréau, P. M. E., et al. (2009). Plasmaspheric density structures and dynamics: Properties observed by the CLUSTER and IMAGE missions. *Space Science Reviews*, *145*(1–2), 55–106. https://doi.org/10.1007/s11214-008-9438-9

Drozdov, A. Y., Allison, H. J., Shprits, Y. Y., Usanova, M. E., Saikin, A., & Wang, D. (2022). Depletions of multi-MeV electrons and their association to minima in phase space density. *Geophysical Research Letters*, *49*(8), e97620. https://doi.org/10.1029/2021GL097620

ELFIN. (2024). Electron Losses and Fields Investigation (ELFIN) Data Archive [Dataset]. *UCLA*. Retrieved from https://data.elfin.ucla.edu/

Gannon, J. L., Li, X., & Heynderickx, D. (2007). Pitch angle distribution analysis of radiation belt electrons based on Combined Release and Radiation Effects Satellite Medium Electrons A data. *Journal of Geophysical Research*, *112*(A5), 5212. https://doi.org/10.1029/2005JA011565

GPS. (2024). Los Alamos National Laboratory CXD data of GPS electron flux [Dataset]. *National Oceanic and Atmospheric Administration*. Retrieved from https://data.elfin.ucla.edu/

Greeley, A. D., Kanekal, S. G., Schiller, Q., Blum, L., Halford, A., Murphy, K., et al. (2024). Persistent pitch angle anisotropies of relativistic electrons in the outer radiation belts. *Journal of Geophysical Research: Space Physics*, *129*(1), e2023JA031549. https://doi.org/10.1029/2023JA031549

Hendry, A. T., Rodger, C. J., & Clilverd, M. A. (2017). Evidence of sub-MeV EMIC-driven electron precipitation. *Geophysical Research Letters*, *44*(3), 1210–1218. https://doi.org/10.1002/2016GL071807

Horne, R. B., Thorne, R. M., Glauert, S. A., Albert, J. M., Meredith, N. P., & Anderson, R. R. (2005). Timescale for radiation belt electron acceleration by whistler mode chorus waves. *Journal of Geophysical Research*, *110*(A3), 3225. https://doi.org/10.1029/2004JA010811

Hua, M., Bortnik, J., & Ma, Q. (2022). Upper limit of outer radiation belt electron acceleration driven by whistler-mode chorus waves. *Geophysical Research Letters*, *49*(15), e2022GL099618. https://doi.org/10.1029/2022GL099618

Jun, C.-W., Miyoshi, Y., Kurita, S., Yue, C., Bortnik, J., Lyons, L., et al. (2021). The characteristics of EMIC waves in the magnetosphere based on the Van Allen Probes and Arase observations. *Journal of Geophysical Research: Space Physics*, *126*(6), e29001. https://doi.org/10.1029/2020JA029001

Kalliokoski, M. M. H., Henderson, M. G., Morley, S. K., Kilpua, E. K. J., Osmane, A., Olifer, L., et al. (2023). Outer radiation belt flux and phase space density response to sheath regions: Van Allen Probes and GPS observations. *Journal of Geophysical Research: Space Physics*, *128*(2), e2022JA030708. https://doi.org/10.1029/2022JA030708

Kennel, C. F. (1969). Consequences of a magnetospheric plasma. *Reviews of Geophysics and Space Physics*, *7*(1–2), 379–419. https://doi.org/10.1029/RG007i001p00379

Kennel, C. F., & Petschek, H. E. (1966). Limit on stably trapped particle fluxes. *Journal of Geophysical Research*, *71*, 1–28. https://doi.org/10.1029/jz071i001p00001

Kersten, T., Horne, R. B., Glauert, S. A., Meredith, N. P., Fraser, B. J., & Grew, R. S. (2014). Electron losses from the radiation belts caused by EMIC waves. *Journal of Geophysical Research: Space Physics*, *119*(11), 8820–8837. https://doi.org/10.1002/2014JA020366

Kim, H.-J., & Chan, A. A. (1997). Fully adiabatic changes in storm time relativistic electron fluxes. *Journal of Geophysical Research*, *102*(A10), 22107–22116. https://doi.org/10.1029/97JA01814

LANL* CODE. (2024). LANL* code [Software]. *LANL*. Retrieved from https://pythonhosted.org/SpacePy/

Li, W., Ma, Q., Thorne, R. M., Bortnik, J., Kletzing, C. A., Kurth, W. S., et al. (2015). Statistical properties of plasmaspheric hiss derived from Van Allen Probes data and their effects on radiation belt electron dynamics. *Journal of Geophysical Research: Space Physics*, *120*(5), 3393–3405. https://doi.org/10.1002/2015JA021048

Li, W., Shen, X. C., Ma, Q., Capannolo, L., Shi, R., Redmon, R. J., et al. (2019). Quantification of energetic electron precipitation driven by plume whistler mode waves, plasmaspheric hiss, and exohiss. *Geophysical Research Letters*, *46*(7), 3615–3624. https://doi.org/10.1029/2019GL082095

Li, W., Shprits, Y. Y., & Thorne, R. M. (2007). Dynamic evolution of energetic outer zone electrons due to wave-particle interactions during storms. *Journal of Geophysical Research*, *112*(A10), 10220. https://doi.org/10.1029/2007JA012368

Li, W., Thorne, R. M., Ma, Q., Ni, B., Bortnik, J., Baker, D. N., et al. (2014). Radiation belt electron acceleration by chorus waves during the 17 March 2013 storm. *Journal of Geophysical Research: Space Physics*, *119*(6), 4681–4693. https://doi.org/10.1002/2014JA019945

Ma, Q., Li, W., Zhang, X.-J., Bortnik, J., Shen, X.-C., Connor, H. K., et al. (2021). Global survey of electron precipitation due to hiss waves in the Earth's plasmasphere and plumes. *Journal of Geophysical Research: Space Physics*, *126*(8), e2021JA029644. https://doi.org/10.1029/2021JA029644

McCollough, J. P., Elkington, S. R., Usanova, M. E., Mann, I. R., Baker, D. N., & Kale, Z. C. (2010). Physical mechanisms of compressional EMIC wave growth. *Journal of Geophysical Research*, *115*(A10), A10214. https://doi.org/10.1029/2010JA015393

Moldwin, M. B., Howard, J., Sanny, J., Bocchicchio, J. D., Rassoul, H. K., & Anderson, R. R. (2004). Plasmaspheric plumes: CRRES observations of enhanced density beyond the plasmapause. *Journal of Geophysical Research*, *109*(A5), 5202. https://doi.org/10.1029/2003JA010320

Morley, S. K., Friedel, R. H. W., Cayton, T. E., & Noveroske, E. (2010). A rapid, global and prolonged electron radiation belt dropout observed with the Global Positioning System constellation. *Geophysical Research Letters*, *37*(6), 6102. https://doi.org/10.1029/2010GL042772

Morley, S. K., Sullivan, J. P., Carver, M. R., Kippen, R. M., Friedel, R. H. W., Reeves, G. D., & Henderson, M. G. (2017). Energetic particle data from the global positioning system constellation. *Space Weather*, *15*(2), 283–289. https://doi.org/10.1002/2017SW001604

Morley, S. K., Sullivan, J. P., Henderson, M. G., Blake, J. B., & Baker, D. N. (2016). The Global Positioning System constellation as a space weather monitor: Comparison of electron measurements with Van Allen Probes data. *Space Weather*, *14*(2), 76–92. https://doi.org/10.1002/2015SW001339

Mourenas, D., Artemyev, A., Agapitov, O., & Krasnoselskikh, V. (2012). Acceleration of radiation belts electrons by oblique chorus waves. *Journal of Geophysical Research*, *117*(A10), 10212. https://doi.org/10.1029/2012JA018041

Mourenas, D., Artemyev, A. V., Agapitov, O. V., Krasnoselskikh, V., & Li, W. (2014). Approximate analytical solutions for the trapped electron distribution due to quasi-linear diffusion by whistler mode waves. *Journal of Geophysical Research: Space Physics*, *119*(12), 9962–9977. https://doi.org/10.1002/2014JA020443

Mourenas, D., Artemyev, A. V., Ma, Q., Agapitov, O. V., & Li, W. (2016). Fast dropouts of multi-MeV electrons due to combined effects of EMIC and whistler mode waves. *Geophysical Research Letters*, *43*(9), 4155–4163. https://doi.org/10.1002/2016GL068921

Mourenas, D., Artemyev, A. V., Zhang, X. J., & Angelopoulos, V. (2022). Extreme energy spectra of relativistic electron flux in the outer radiation belt. *Journal of Geophysical Research: Space Physics*, *127*(11), e2022JA031038. https://doi.org/10.1029/2022JA031038

Mourenas, D., Artemyev, A. V., Zhang, X. J., & Angelopoulos, V. (2023). Upper limit on outer radiation belt electron flux based on dynamical equilibrium. *Journal of Geophysical Research: Space Physics*, *128*(8), e2023JA031676. https://doi.org/10.1029/2023JA031676

Mourenas, D., Artemyev, A. V., Zhang, X. J., & Angelopoulos, V. (2024). Checking key assumptions of the Kennel-Petschek flux limit with ELFIN CubeSats. *Journal of Geophysical Research: Space Physics*, *129*(2), e2023JA032193. https://doi.org/10.1029/2023JA032193

Mourenas, D., Artemyev, A. V., Zhang, X. J., Angelopoulos, V., Tsai, E., & Wilkins, C. (2021). Electron lifetimes and diffusion rates inferred from ELFIN measurements at low altitude: First results. *Journal of Geophysical Research: Space Physics*, *126*(11), e29757. https://doi.org/10.1029/2021JA029757

Mourenas, D., Ma, Q., Artemyev, A. V., & Li, W. (2017). Scaling laws for the inner structure of the radiation belts. *Geophysical Research Letters*, *44*(7), 3009–3018. https://doi.org/10.1002/2017GL072987

Ni, B., Cao, X., Zou, Z., Zhou, C., Gu, X., Bortnik, J., et al. (2015). Resonant scattering of outer zone relativistic electrons by multiband EMIC waves and resultant electron loss time scales. *Journal of Geophysical Research: Space Physics*, *120*(9), 7357–7373. https://doi.org/10.1002/2015JA021466

O'Brien, T. P., & Moldwin, M. B. (2003). Empirical plasmapause models from magnetic indices. *Geophysical Research Letters*, *30*(4), 1152. https://doi.org/10.1029/2002GL016007

Olifer, L., Mann, I. R., Ozeke, L. G., Claudepierre, S. G., Baker, D. N., & Spence, H. E. (2021). On the similarity and repeatability of fast radiation belt loss: Role of the last closed drift shell. *Journal of Geophysical Research: Space Physics*, *126*(11), e2021JA029957. https://doi.org/10.1029/2021JA029957

Ozeke, L. G., Mann, I. R., Olifer, L., Claudepierre, S. G., Spence, H. E., & Baker, D. N. (2022). Statistical characteristics of energetic electron pitch angle distributions in the Van Allen Probe era: 1. Butterfly distributions with flux peaks at preferred pitch angles. *Journal of Geophysical Research: Space Physics*, *127*(3), e2021JA029907. https://doi.org/10.1029/2021JA029907

Pinto, V. A., Zhang, X.-J., Mourenas, D., Bortnik, J., Artemyev, A. V., Lyons, L. R., & Moya, P. S. (2020). On the confinement of ultrarelativistic electron remnant belts to low L shells. *Journal of Geophysical Research: Space Physics*, *125*(3), e27469. https://doi.org/10.1029/2019JA027469

Remya, B., Sibeck, D. G., Halford, A. J., Murphy, K. R., Reeves, G. D., Singer, H. J., et al. (2018). Ion injection triggered EMIC waves in the Earth's magnetosphere. *Journal of Geophysical Research: Space Physics*, *123*(6), 4921–4938. https://doi.org/10.1029/2018JA025354

Roederer, J. G. (1970). *Dynamics of geomagnetically trapped radiation*. Springer. https://doi.org/10.1007/978-3-642-49300-3

Ross, J. P. J., Glauert, S. A., Horne, R. B., Watt, C. E. J., & Meredith, N. P. (2021). On the variability of EMIC waves and the consequences for the relativistic electron radiation belt population. *Journal of Geophysical Research: Space Physics*, *126*(12), e29754. https://doi.org/10.1029/2021JA029754

Saikin, A. A., Zhang, J.-C., Allen, R. C., Smith, C. W., Kistler, L. M., Spence, H. E., et al. (2015). The occurrence and wave properties of H^+-He^+-O^+-band EMIC waves observed by the Van Allen Probes. *Journal of Geophysical Research: Space Physics*, *120*(9), 7477–7492. https://doi.org/10.1002/2015JA021358

Sandanger, M., Søraas, F., Aarsnes, K., Oksavik, K., & Evans, D. S. (2007). Loss of relativistic electrons: Evidence for pitch angle scattering by electromagnetic ion cyclotron waves excited by unstable ring current protons. *Journal of Geophysical Research*, *112*(A12), A12213. https://doi.org/10.1029/2006JA012138

Schulz, M., & Lanzerotti, L. J. (1974). *Particle diffusion in the radiation belts*. Springer. https://doi.org/10.1007/978-3-642-65675-0

Shekhar, S., Millan, R., & Smith, D. (2017). A statistical study of the spatial extent of relativistic electron precipitation with polar orbiting environmental satellites. *Journal of Geophysical Research: Space Physics*, *122*(11), 11274–11284. https://doi.org/10.1002/2017JA024716

Shi, R., Summers, D., Ni, B., Fennell, J. F., Blake, J. B., Spence, H. E., & Reeves, G. D. (2016). Survey of radiation belt energetic electron pitch angle distributions based on the Van Allen Probes MagEIS measurements. *Journal of Geophysical Research: Space Physics*, *121*(2), 1078–1090. https://doi.org/10.1002/2015JA021724

Shi, X., Artemyev, A., Zhang, X.-J., Mourenas, D., An, X., & Angelopoulos, V. (2024). Properties of intense H-band electromagnetic ion cyclotron waves: Implications for quasi-linear, nonlinear, and nonresonant wave-particle interactions. *Journal of Geophysical Research: Space Physics*, *129*(1), e2023JA032179. https://doi.org/10.1029/2023JA032179

Shprits, Y. Y., Kellerman, A., Aseev, N., Drozdov, A. Y., & Michaelis, I. (2017). Multi-MeV electron loss in the heart of the radiation belts. *Geophysical Research Letters*, *44*(3), 1204–1209. https://doi.org/10.1002/2016GL072258

Shprits, Y. Y., Thorne, R. M., Friedel, R., Reeves, G. D., Fennell, J., Baker, D. N., & Kanekal, S. G. (2006). Outward radial diffusion driven by losses at magnetopause. *Journal of Geophysical Research*, *111*(A11), 11214. https://doi.org/10.1029/2006JA011657

Shue, J.-H., Song, P., Russell, C. T., Steinberg, J. T., Chao, J. K., Zastenker, G., et al. (1998). Magnetopause location under extreme solar wind conditions. *Journal of Geophysical Research*, *103*(A8), 17691–17700. https://doi.org/10.1029/98JA01103

Su, Z., Liu, N., Zheng, H., Wang, Y., & Wang, S. (2018). Large-amplitude extremely low frequency hiss waves in plasmaspheric plumes. *Geophysical Research Letters*, *45*(2), 565–577. https://doi.org/10.1002/2017GL076754

Summers, D., & Thorne, R. M. (2003). Relativistic electron pitch-angle scattering by electromagnetic ion cyclotron waves during geomagnetic storms. *Journal of Geophysical Research*, *108*(A4), 1143. https://doi.org/10.1029/2002JA009489

Thorne, R. M., & Kennel, C. F. (1971). Relativistic electron precipitation during magnetic storm main phase. *Journal of Geophysical Research*, *76*(19), 4446–4453. https://doi.org/10.1029/JA076i019p04446

Tsyganenko, N. A., & Sitnov, M. I. (2005). Modeling the dynamics of the inner magnetosphere during strong geomagnetic storms. *Journal of Geophysical Research*, *110*(A3), A03208. https://doi.org/10.1029/2004JA010798

Turner, D. L., Angelopoulos, V., Li, W., Hartinger, M. D., Usanova, M., Mann, I. R., et al. (2013). On the storm-time evolution of relativistic electron phase space density in Earth's outer radiation belt. *Journal of Geophysical Research: Space Physics*, *118*(5), 2196–2212. https://doi.org/10.1002/jgra.50151

Usanova, M. E., Drozdov, A., Orlova, K., Mann, I. R., Shprits, Y., Robertson, M. T., et al. (2014). Effect of EMIC waves on relativistic and ultrarelativistic electron populations: Ground-based and Van Allen Probes observations. *Geophysical Research Letters*, *41*(5), 1375–1381. https://doi.org/10.1002/2013GL059024

Usanova, M. E., Mann, I. R., Rae, I. J., Kale, Z. C., Angelopoulos, V., Bonnell, J. W., et al. (2008). Multipoint observations of magnetospheric compression-related EMIC Pc1 waves by THEMIS and CARISMA. *Geophysical Research Letters*, *35*(17), L17S25. https://doi.org/10.1029/2008GL034458

WDC FOR GEOMAGNETISM. (2024). Geomagnetic indices [Dataset]. *WDC for Geomagnetism*. Retrieved from https://wdc.kugi.kyoto-u.ac.jp/wdc/Sec3.html

West, H. I., Jr. (1979). The signatures of the various regions of the outer magnetosphere in the pitch angle distributions of energetic particles. *Washington DC American Geophysical Union Geophysical Monograph Series*, *21*, 150–179. https://doi.org/10.1029/GM021p0150

Wong, J.-M., Meredith, N. P., Horne, R. B., Glauert, S. A., & Ross, J. P. J. (2024). New chorus diffusion coefficients for radiation belt modeling. *Journal of Geophysical Research: Space Physics*, *129*(1), e2023JA031607. https://doi.org/10.1029/2023JA031607

Xiang, Z., Tu, W., Li, X., Ni, B., Morley, S. K., & Baker, D. N. (2017). Understanding the mechanisms of radiation belt dropouts observed by Van Allen Probes. *Journal of Geophysical Research: Space Physics*, *122*(10), 9858–9879. https://doi.org/10.1002/2017JA024487

Xiang, Z., Tu, W., Ni, B., Henderson, M. G., & Cao, X. (2018). A statistical survey of radiation belt dropouts observed by Van Allen Probes. *Geophysical Research Letters*, *45*(16), 8035–8043. https://doi.org/10.1029/2018GL078907

Yu, Y., Koller, J., Zaharia, S., & Jordanova, V. (2012). *L** neural networks from different magnetic field models and their applicability. *Space Weather*, *10*(2), S02014. https://doi.org/10.1029/2011SW000743

Zhang, W., Ni, B., Huang, H., Summers, D., Fu, S., Xiang, Z., et al. (2019). Statistical properties of hiss in plasmaspheric plumes and associated scattering losses of radiation belt electrons. *Geophysical Research Letters*, *46*(11), 5670–5680. https://doi.org/10.1029/2018GL081863

Zhang, X. J., Li, W., Ma, Q., Thorne, R. M., Angelopoulos, V., Bortnik, J., et al. (2016). Direct evidence for EMIC wave scattering of relativistic electrons in space. *Journal of Geophysical Research: Space Physics*, *121*(7), 6620–6631. https://doi.org/10.1002/2016JA022521

Zhang, X.-J., Li, W., Thorne, R. M., Angelopoulos, V., Bortnik, J., Kletzing, C. A., et al. (2016). Statistical distribution of EMIC wave spectra: Observations from Van Allen Probes. *Geophysical Research Letters*, *43*(24), 12. https://doi.org/10.1002/2016GL071158

Zhang, X.-J., Mourenas, D., Artemyev, A. V., Angelopoulos, V., & Thorne, R. M. (2017). Contemporaneous EMIC and whistler mode waves: Observations and consequences for MeV electron loss. *Geophysical Research Letters*, *44*(16), 8113–8121. https://doi.org/10.1002/2017GL073886

Zhang, X.-J., Mourenas, D., Shen, X.-C., Qin, M., Artemyev, A. V., Ma, Q., et al. (2021). Dependence of relativistic electron precipitation in the ionosphere on EMIC wave minimum resonant energy at the conjugate equator. *Journal of Geophysical Research: Space Physics*, *126*(5), e2021JA029193. https://doi.org/10.1029/2021JA029193

Zhao, H., Friedel, R. H. W., Chen, Y., Reeves, G. D., Baker, D. N., Li, X., et al. (2018). An empirical model of radiation belt electron pitch angle distributions based on Van Allen Probes measurements. *Journal of Geophysical Research: Space Physics*, *123*(5), 3493–3511. https://doi.org/10.1029/2018JA025277